

This is the accepted manuscript made available via CHORUS. The article has been published as:

Visualizing anisotropic propagation of stripe domain walls in staircaselike transitions of IrTe_2

Tobias Maurer, Matthias Vogt, Pin-Jui Hsu, Gheorghe Lucian Pascut, Kristjan Haule, Valery Kiryukhin, Junjie Yang, Sang-Wook Cheong, Weida Wu, and Matthias Bode

Phys. Rev. B **94**, 014106 — Published 11 July 2016

DOI: [10.1103/PhysRevB.94.014106](https://doi.org/10.1103/PhysRevB.94.014106)

Visualizing Anisotropic Propagation of Stripe Domain Walls in Staircase-Like Transitions of IrTe₂

Tobias Maurer,¹ Matthias Vogt,¹ Pin-Jui Hsu,¹ Gheorghe Lucian Pascut,² Kristjan Haule,²
Valery Kiryukhin,² Junjie Yang,³ Sang-Wook Cheong,^{2,3} Weida Wu,² and Matthias Bode^{1,4}

¹*Physikalisches Institut, Experimentelle Physik II,
Universität Würzburg, 97074 Würzburg, Germany*

²*Rutgers Center for Emergent Materials and Department of Physics and Astronomy,
Rutgers University, Piscataway, New Jersey 08854, USA*

³*Laboratory for Pohang Emergent Materials and Department of Physics,
Pohang University of Science and Technology,
Pohang 790-784, Republic of Korea*

⁴*Wilhelm Conrad Röntgen-Center for Complex Material Systems (RCCM),
Universität Würzburg, Am Hubland, 97074 Würzburg, Germany*

(Dated: June 20, 2016)

Abstract

We present a scanning tunneling microscopy (STM) study of the domain evolution across two first-order phase transitions of stripe modulations in IrTe₂ that occur at $T_C \approx 275$ K and $T_S \approx 180$ K, respectively. Phase coexistence of the hexagonal (1×1) structure and the (5×1) stripe modulation is observed at T_C , while various ($p \times 1$) modulations ($p = 3n + 2$ with $2 \leq n \in \mathbb{N}$) are observed below T_S . Using STM atomic resolution, we observe anisotropic propagation of domain boundaries along different directions, indicating significantly different kinetic energy barriers. These results are consistently explained by a theoretical analysis of the energy barrier for domain wall propagation as obtained by density functional theory. Individual switching processes observed by STM indicate that the wide temperature range of the transition from the (5×1) stripes to the (6×1)-ordered ground state is probably caused by the numerically limited subset of switching processes that are allowed between a given initial and the final state. The observations on IrTe₂ are discussed in terms of a “harmless staircase” with a finite number of first-order transitions between commensurate phases and within a “dynamical freezing” scenario.

I. INTRODUCTION

A. Solid–solid phase transition

Many of today’s functionalities such as conductivity switching in correlated materials, magnetization/polarization switching in multiferroic, ferroelectric and pyroelectric materials,¹ and the switching between non-polarized and spin-polarized bands in strongly spin-orbit-coupled materials,² are associated with the presence of solid–solid phase transition (SSPT) between different crystalline structures. Understanding the atomistic details of the underlying mechanisms that occur during SSPTs at a level beyond the existing knowledge based on the classifications of phase transitions, e.g. within the Ehrenfest’s thermodynamic or more modern classifications, is mandatory for the design and the discovery of novel phases of matter with desired macroscopic functionalities.^{3,4}

Ehrenfest’s simple view of first- and second-order (1st- and 2nd-order) phase transitions is based on the different behavior of the thermodynamic free energy and its first derivative, usually called order parameter. While it changes abruptly at T_C for 1st-order phase transitions, the order parameter varies continuously for 2nd-order phase transitions. The modern view of the 1st- and 2nd-order phase transitions is based on an examination of the latent heat during the phase transition. In particular, for SSPTs the classification effectively reduces to an analysis of the pathways the crystal’s atomic configurations take during the transition. For a 2nd-order (or weakly 1st-order) SSPT the structural changes taking place across the phase transition are small enough to only slightly alter the chemical bonds. As a consequence, there is none or very little latent heat and discontinuities of physical quantities associated with this transition are small. In contrast, the structural changes associated with atomic displacements of strongly 1st-order SSPTs are of the order of the lattice parameters, thus breaking the chemical bonds. As a result, there are drastic changes in the physical quantities at the transition point, giving rise to a large latent heat and thermal hysteresis (phase coexistence).

Although, a microscopic picture of 1st- and 2nd-order phase transitions was achieved using spatially averaging experimental probes (such as x-ray/neutron scattering) and phenomenological Landau theory, an atomistic understanding of the transition mechanisms became possible only during the past decade after advanced molecular dynamics simulations

and modeling approaches were developed.^{5–10} Up to the present, simulations have largely focussed on establishing atomistic mechanisms for some pressure-induced phase transitions in ionic and semi-conductor materials.^{5–8,11,12} Summarizing the results in simple terms, these simulations showed that the growth of the new phase at the domain–domain interface either proceeds by (i) atomic reorganizations or (ii) via a new metastable phase.^{5,11,13–16}

Due to the lack of materials with slow dynamics and due to the difficulty of performing experiments to test such theories, however, these predictions have so far been verified by a very small number of experiments only.^{17–19} As we will show below, the strongly spin-orbit-coupled $5d$ transition metal dichalcogenide IrTe_2 is one of the very few systems with a 1st-order phase transition that is slow enough to allow for studying its dynamics by scanning tunneling microscopy on a single uni cell level. Recently, intense studies of IrTe_2 have shown,^{20–34} that the covalent character of the Ir–Ir and Ir–Te bonds is responsible for its complex behavior during phase transitions,^{28,34} for the unusual two-dimensional Fermi surfaces,^{2,28,35} and for the spin-polarized bands found in some of its metastable phases.² Indeed, our results reveal that both scenarios (i) and (ii) mentioned above take place in IrTe_2 . These results provides us with high-resolution real space data yet unavailable for the structural features during dynamic phase transition processes. Understanding of the nature of the metastable phases in this material, could lead to new ideas of materials synthesis, where the switching between non-polarized and spin-polarized bands could be achieved in bulk or monolayers.

B. Properties of IrTe_2

Transport measurements of IrTe_2 show a magnetic susceptibility drop and resistivity increase at $T_C \approx 275\text{K}$ upon cooling.^{20,21} Since a relatively large hysteresis was observed it could already early be assigned to a first-order phase transition.^{20,21} Electron- and X-ray diffraction (XRD) measurements show that this phase transition is accompanied by a structural transition from a trigonal ($P\bar{3}m1$) to a triclinic ($P\bar{1}$) lattice²⁸ and the appearance of a new lattice modulation with the wave vector $q = \frac{1}{5}(1, 0, \bar{1})$.²²

Surprisingly, later transport measurements performed on more perfect crystals revealed the existence of a second phase transition at $T_S = 180\text{ K}$, which is characterized by a sudden increase of the electrical resistivity, ρ , followed by an approximately linear reduction down

to $T \approx 50$ K [see Fig. 1(a) in Ref. 27]. Temperature-dependent STM measurements indicated that this second phase transition is caused by the steady melting of a soliton lattice that involves the appearance of new periodicities.²⁷ While at $T_C > T > T_S$ the surface exhibits a rather homogeneous stripe pattern with a (5×1) unit cell, corresponding to the above-mentioned wave vector $q = \frac{1}{5}(1, 0, \bar{1})$ found in reciprocal space, cooling to $T \leq T_S$ leads to the appearance of $(p \times 1)$ -ordered areas ($p = 3n + 2$ with $2 \leq n \in \mathbb{N}$).²⁷

These modulations consist of two types of fundamental units, i.e. blocks with an integer number of $3a^*$ atomic columns that are separated by a single $2a^*$ unit, where a^* represents the inter-column spacing of ≈ 3.4 Å. It was found that the density of $2a^*$ units, coined solitons in Ref. 27, slowly decreases with decreasing temperature, eventually resulting in a (6×1) -ordered ground state. The existence of a second IrTe₂ phase was confirmed by several studies.^{29–33,36} For example, XRD data of IrTe₂ at $T_S = 100$ K reported on the existence of $q = 1/8$ stripe phase.³¹ Furthermore, low-temperature measurements consistently reported the observation of six-fold superstructures,^{33,36} although the (6×1) -ordered ground state was misinterpreted as a (3×1) structure in Ref. 32.

In spite of the general agreement on the existence of low-temperature commensurate superstructures in IrTe₂, the physical mechanism responsible for their formation is still under debate. Originally Fermi surface nesting was proposed to be the driving force,²¹ but later experimental results indicated irregularities inconsistent with Fermi surface nesting.^{23–25} Alternatively, the local bonding states of Te orbitals and the mixed valence nature of Ir ions may induce charge modulations.^{22,26,29} This scenario was also supported by high-resolution STM images which show dimerization of Te atoms on the surface.²⁷ Furthermore, the observed series of hierarchically modulated stripe phases has been ascribed to intralayer Ir–Ir dimerization that competes with interlayer Te–Te bonding.³³ It has also been proposed that the spatial modulations of the electronic density of states have to be distinguished from structural distortions as they appear independently.³³

In this contribution we present a real-space STM study of the phase transitions in IrTe₂. We show that the first transition at T_C proceeds discontinuously, verifying its first-order nature. We examine the processes that determine the propagation of domain boundaries (DBs) at T_S and discover anisotropic propagation speeds of differently oriented DBs. These results are explained by a kinetic energy barrier analysis using density functional theory (DFT). The slow dynamics of $(p \times 1)$ stripes in IrTe₂ shed new light on the emergent

complex energy landscape of this material. Furthermore, we present evidence that the wide temperature range of the transition from the (5×1) stripes to the ground state may be caused by the numerically limited subset of switching processes that are allowed between a given initial and the final state. We speculate that our data obtained on IrTe₂ potentially represent the first direct observation of a “harmless staircase”, which is characterized by a finite number of first-order transitions between commensurate (C) phases and which was originally postulated for oscillating soliton interactions.³⁷ Alternatively, the data may also represent “dynamical freezing”,³⁸ potentially caused by the complex energy landscape of IrTe₂.

II. EXPERIMENTAL SETUP AND PROCEDURES

IrTe₂ single crystals were grown by the self-flux method.²¹ STM experiments were performed with electro-chemically etched tungsten tips in a variable-temperature (VT-)STM system (temperature range: $50 \text{ K} < T < 330 \text{ K}$) in an ultra-high vacuum (UHV) system with a base pressure $p \leq 10^{-10}$ mbar. Clean (001) surfaces were obtained by cleaving IrTe₂ crystals under UHV conditions at room temperature (RT) just before insertion into the sample stage. Topographic STM images were taken in the constant-current mode at typical scan parameters of $U = 0.1 \dots 0.5 \text{ V}$ and $I = 0.1 \dots 1 \text{ nA}$. STM images were analyzed with the WSxM software.³⁹ Kinetic barriers of domain wall propagation were analyzed with DFT using the WIEN2k code.⁴⁰

III. RESULTS AND DISCUSSION

A. The first phase transition at T_C

Figure 1(a) shows an STM overview image of a cleaved $\text{IrTe}_2(001)$ surface close to the first phase transition (T_C) on cooling. While the right part is essentially flat as indicated by its constant color and brightness, a significant gradient can clearly be recognized in the left part of the image. This gradient is accompanied by the appearance of a (5×1) stripe pattern as shown in the higher resolution image of Fig. 1(b). As a result of the trigonal crystalline symmetry of the material three equivalent orientations can be found on the crystal surface (not shown here), with stripes running along the $[100]$, $[010]$, or the $[110]$ direction, i.e. rotated by 120° . The bottom panel of Fig. 1(a) shows a line section taken at the bottom of the STM image. It reveals a tilt between the two parts of the image. Although quantification is complicated by thermal drift and the rapid temporal evolution of the surface, resulting in

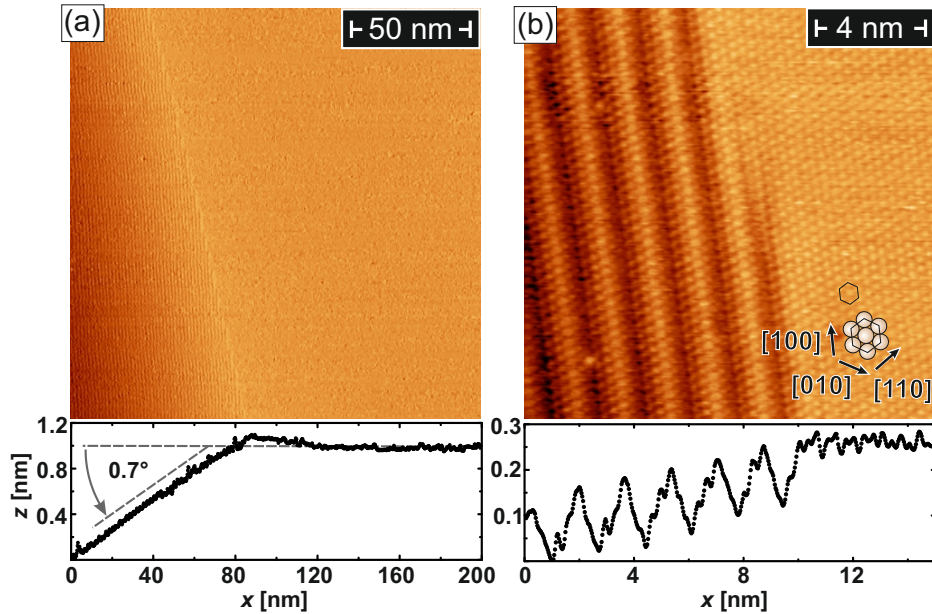


FIG. 1. (Color online) (a) Overview STM image of a $\text{IrTe}_2(001)$ surface at the first phase transition on cooling. A line section taken at the bottom of the STM image reveals a tilt of 0.7° . (b) A zoomed-in image of the transition region (top panel) identifies the position of the kink as the boundary between the (1×1) (right) and the (5×1) phase (left). The enhanced corrugation of the (5×1) phase can be recognized in the line section (bottom panel).

a relatively large error, straightforward trigonometry results in a tilt angle of $0.7 \pm 0.3^\circ$, in reasonable agreement with the value ($\sim 0.3^\circ$) estimated from structural data in Ref. 28.

B. The second phase transition at T_S

Typical sizes of q -domains (one stripe orientation) are much larger than the STM scan range.²⁷ Therefore, most STM images show a single domain only without any DB. To capture the DB motion at the second phase transition the x - y -coarse motion stage was employed for macroscopically changing the scanned surface area. This procedure was repeated at 190 K, i.e. well above T_S , until a DB was located. As confirmed by several successive images this DB did not show any tendency of creep motion or domain wall movement, possibly because it was stabilized by surface or bulk dislocations. Then the sample temperature was lowered gradually while monitoring the DB and adjusting for the temperature-induced drift of the crystal. Only when the sample was cooled to $T = 180$ K a significant domain wall motion was observed and the subsequent evolution of domains and DBs was recorded (see Supplemental Material for a movie of the complete data set).

The top panel of Fig. 2(a) shows the initial STM image of a DB which separates a (5×1) -ordered domain (right) from a domain that is dominated by the (8×1) modulation (left). The respective superstructures are highlighted by color-coding in the bottom panel of Fig. 2. Interestingly, the DB exhibits two different directions that are marked by arrows and labeled **A** and **B** in Fig. 2(a). While the (8×1) modulation runs parallel to the DB for **A**, the stripe's super-modulations are cut under an angle of about 60° in **B**. The differently oriented DBs **A** and **B** intersect at the position of a double-line which is labeled **d** and probably represents two linear defects in the (5×1) -ordered domain. Some selected images taken after 26, 52, and 78 min are shown in Fig. 2(b)-(d), respectively. Note that the position of a point-like defect, which is labeled by a circle in all panels, serves as a land mark.

The evolution captured in this sequence is typical for the domain evolution at the 2nd transition which was found to take place on a time scale of several hours after stabilizing the sample temperature. In this particular case the left domain, which originally consists of (8×1) and higher p modulations, expands at a speed $v \approx 1$ nm/min along the defect line **d** towards the bottom right side of the image, thereby reducing the area of the (5×1) -ordered domain. Rough analysis of the images presented in Fig. 2(a)-(d) already reveals that the

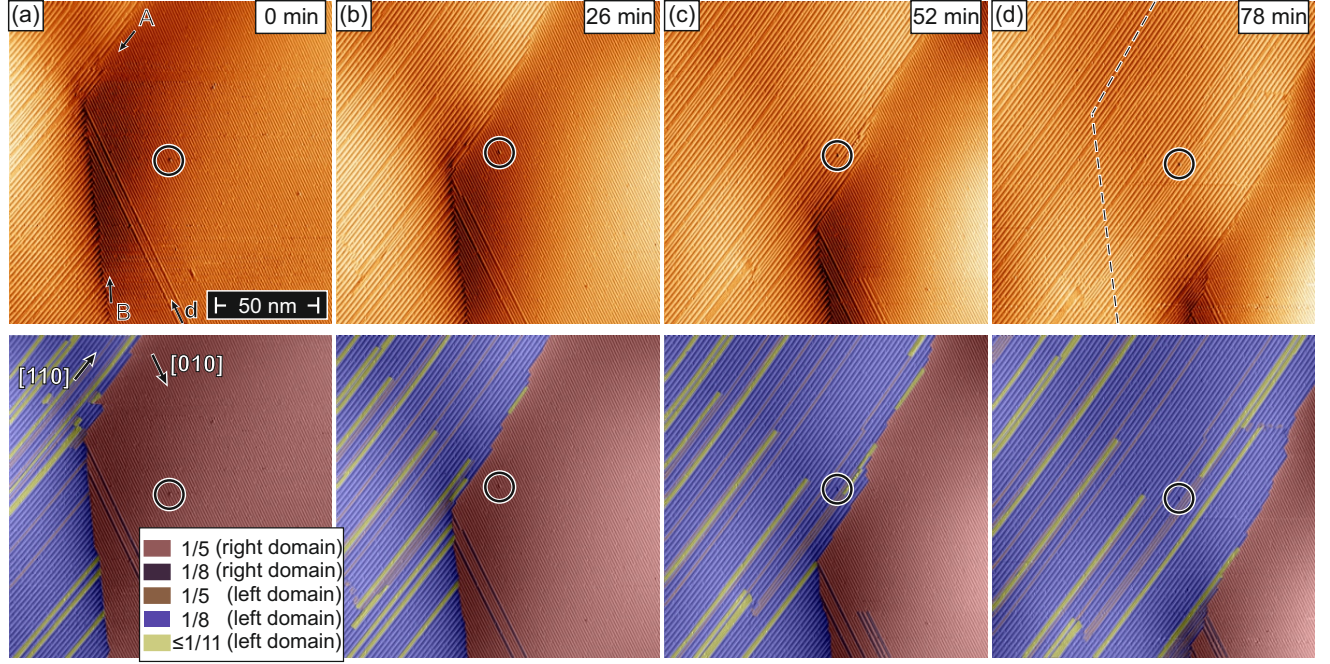


FIG. 2. (Color online) (a) STM topographic image taken at $T_S = 180$ K. Different $(p \times 1)$ -ordered areas ($p = 3n + 2$ with $n \in \mathbb{N}$) are color-enhanced in the bottom panel. A domain boundary (DB) separates a (5×1) domain (right) from a domain dominated by (8×1) modulations (left). It consists of two differently oriented straight segments, marked A and B. A circular label marks a defect to provide a reference point. The temporal evolution of the domain structure is shown after (b) 26, (c) 52, and (d) 78 min. The original position of the DB is highlighted by a line in (d).

growth of the (8×1) modulation takes place by slow movement of the DB marked **B** to the right. As soon as the stripes of the (8×1) domain cross the double-line defect **d** they quickly propagate towards the right.

Figure 3 displays the growth of modulation stripes at higher spatial and temporal resolution. Because the movement of stripes takes place on very different time scales, depending on whether they are oriented under some angle or parallel to the DB, the time increments between the panels in Figs. 3(a) and (b) also differ by about one order of magnitude. The top panel of Fig. 3(a) shows the initial configuration (0 min) of two stripe domains which are both oriented at an angle of about 30° with respect to the DB. A DB separates the (5×1) domain with stripes along the $[010]$ direction (right part of the image) from a (8×1) -dominated domain with modulations along the $[110]$ direction (left). As verified by two point-like defects marked by circles, the middle and bottom panel of Fig. 3(a) depict the

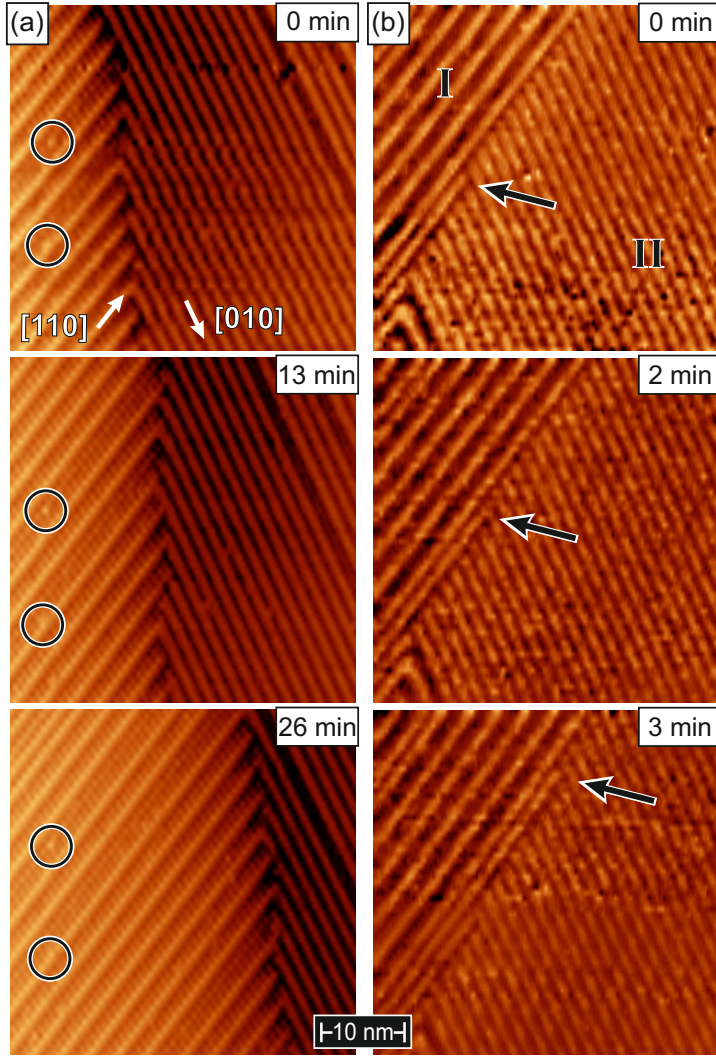


FIG. 3. (Color online) (a) Series of STM images at $T_S = 180$ K showing the growth of modulation stripes oriented at an angle of about 60° with respect to the DB. Two surface defects are marked to provide a reference point. (b) Image series of the line-by-line domain growth of stripes running parallel to the DB. The arrow indicates the termination point of the same line. The average growth velocity of a single stripe is much higher than in (a).

same surface area 13 and 26 min later, respectively. Detailed comparison reveals that the left domain expands by occasional and discontinuous jumps along the $[110]$ direction. At the long-term average the motion of this DB proceeds at a pace of about 1 nm/min.

In contrast, the movement of stripes oriented parallel to a DB proceeds at a much higher speed. The top panel of Fig. 3(b) shows a region where the stripes of the domain in the upper left part of the image (domain I) are oriented along the DB (see Supplemental Material for a movie of the complete data set). In the lower part of the image another domain (labeled II) exists with modulation stripes that are oriented under an angle of about 60° with respect to the DB. In the initial configuration (0 min) we image a semi-infinite modulation line (marked by an arrow). In general, we find that the termination points of such lines are always located at the minimum between two modulations of domain II. In the subsequent images we observed the discontinuous propagation of this line along the direction of the DB.

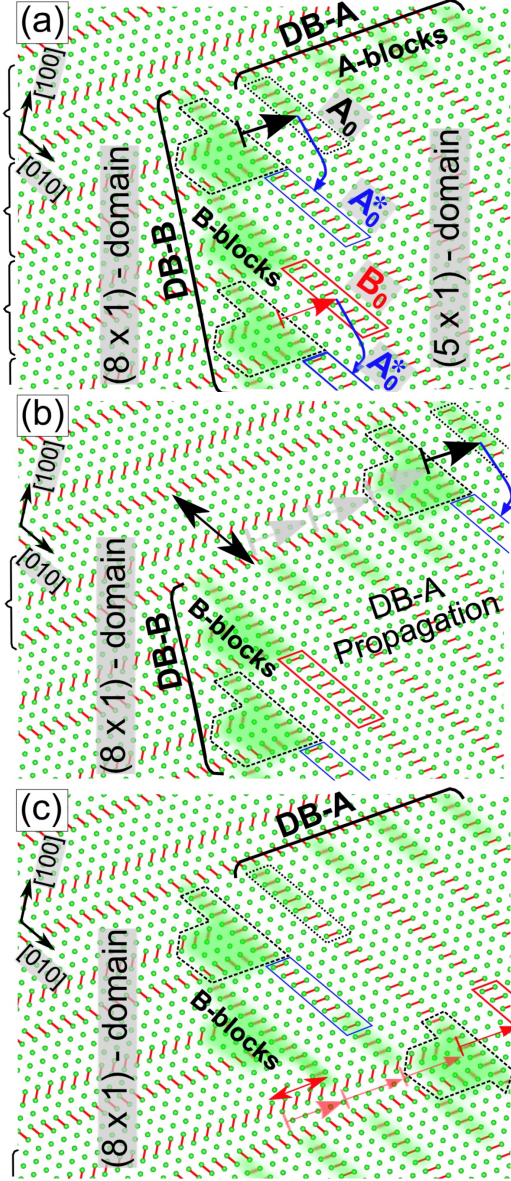


FIG. 4. (Color online) (a) Schematic representation of the DB between the (8×1) (left) and (5×1) (right) phases. Two orientations, DB-A and DB-B (emphasized by round brackets) and their broken dimers, labeled “A-” (dotted line) and “B-blocks” (dashed), are marked green. Blue and black/red arrows represent tunneling processes of “A-” and “B-blocks”, respectively, with their size being inversely proportional to the potential barrier height. Parallelograms represent regions affected by structural changes during the tunneling processes. (b) Snapshot of the DB-B propagation after three tunneling processes (gray arrows). The double black arrow indicates the spatial movement of DB-A within one step. (c) Alternative propagation of DB-B. The double red arrow shows movement of DB-B within one step.

Within the time resolution of our STM measurements ($\approx 0.1 \dots 1$ s between successive scan lines) it appears to consist of abrupt jumps that extend over discrete distances equivalent to integer multiples of the line separation. In the absence of pinning at defects we find average propagation speeds of about 5 nm/min at 180 K. For example, within the 3 min that elapsed between the top and the bottom image of Fig. 3(b) the line marked by an arrow covered a distance of 17 ± 2 nm. This higher speed is likely caused by the fact that an extension of the stripe is associated with a lower barrier height, as indicated by the following analysis.

C. DFT simulations

In order to explain the mechanisms and understand the respective movement of **A**- and **B**-type DBs, we estimated the potential barrier height by DFT simulations. Together with geometrical considerations this potential barrier, which determines the tunneling rate of the DB, is used to explain the mechanism of DB propagation and show how the movement of the two boundaries **A** and **B** are correlated. Fig. 4 shows the crystal structure of (8×1) (left) and (5×1) (right) phases. Green dots mark positions of Ir atoms, red bonds indicate the two Ir atoms within a dimer. The intra-dimer Ir-Ir distance amounts to approximately $\sim 3.1 \text{ \AA}$, while the inter-dimer distance within the stripes is very close to the undimerized distance between Ir atoms of $\sim 3.9 \text{ \AA}$.^{28,31} Surface layer Te atoms are not shown for clarity. Note that the stability of the dimerized phases is governed by the competition between the energy gain due to Ir dimerization and the elastic energy penalty due to the deformation of the IrTe_6 octahedra.³¹ The DB results in regions of broken dimers, which we marked by blurred green color. To estimate the size of the region with broken dimers, we performed DFT structural relaxations within a large supercell of the (5×1) phase and determine that approximately three dimers are broken before the dimerized stripe heals (see Supplemental Material for details of the calculations).

Based on our simulation and geometric consideration, Fig. 4(a) and (b) shows how **A**- and **B**-type DBs propagate. The difference between the two panels corresponds to three typical steps during domain propagation. Within each step, the top left **B**-block moves to the right ($[110]$ direction). Simultaneously the corresponding **A**-block moves in the $[010]$ direction [black/blue arrows in (a)]. Once the top left **B**-block moves for a few steps and cuts (5×1) stripes [gray arrows in (b)], the next **B**-block follows, creating a correlated **A** and **B** DB propagation. To understand why the top left **B**-block moves first in the $[110]$ direction, a process which corresponds to the fast movement experimentally observed in Fig. 3(b), we notice that this change generates the smallest number of newly broken bonds per unit area, as many bonds on its path along the junction of (5×1) and (8×1) stripes at the domain boundary-**A** were already broken before [**A**-blocks in Fig. 4(a)]. More precisely, within one step only eight new dimers of the (5×1) phase are required to break, five within the **A**₀-block and three within the new **A**₀^{*}-block. DFT simulations show that the energy barrier which needs to be overcome for breaking each dimer in either the (5×1) or the

(8×1) phase amounts to several meV.

Fig. 4(c) shows an alternative domain wall propagation corresponding to the situation observed in Fig. 3(a). In this case a **B**-block somewhere in a B-type domain wall moves to the right while the top **B**-block remains at its original position. In contrast to the situation sketched before, this movement not only requires the breaking of the (5×1) stripe marked **B**₀ [red square in Fig. 4(a)] but also creates another **A**₀^{*}-block just below, resulting in a total of eleven newly broken dimers. It is reasonable to assume that this larger number of dimers also results in a larger energy barrier for DB movement and, therefore, to slower propagation, in qualitative agreement with the experimental observations.

D. Discussion

The measurements shown in Fig. 5 give some clues of the processes that occur during the so-called soliton melting process. It displays subsequently recorded color-enhanced STM images showing the same surface area at a sample temperature $T = 180$ K upon cooling. At the beginning, Fig. 5(a), a large (5×1) -ordered domain with stripes along the $[100]$ direction can be found on the right side of the image. In contrast, the left side of the image is governed by $(p \times 1)$ stripes with $p = 3n + 2$ that are oriented along the $[110]$ direction. Since the data were taken during the cooling process we can expect that the latter domain will expand on the expense of the former. In fact, Figs. 5(b) and (c) show an evolution of the region around the DB that is similar to processes discussed in relation to Fig. 3(b) above, i.e. the movement of stripes that are oriented parallel with respect to a DB.

In addition, some characteristic changes are observed that take place in the area marked by a rectangle ($\approx 25 \times 12$ nm²). As emphasized by the color-coding, by going from the left to the right of this surface area in Fig. 5(a) we find (8×1) - (purple), (11×1) - (yellow), and (5×1) -ordered domains (brown) to coexist in close proximity. Between Figs. 5(a) and (b) this configuration abruptly changes. In particular, over a length of about 10 nm the previously existing (11×1) stripe and a neighboring (5×1) stripe have converted into two (8×1) stripes, thereby extending the (8×1) domain. Interestingly, this extension then quickly propagates to the upper right [see Fig. 5(c)] such that the (11×1) stripe in the upper part of the image is eventually annihilated and the (8×1) domain extends over a larger part of the sample surface.

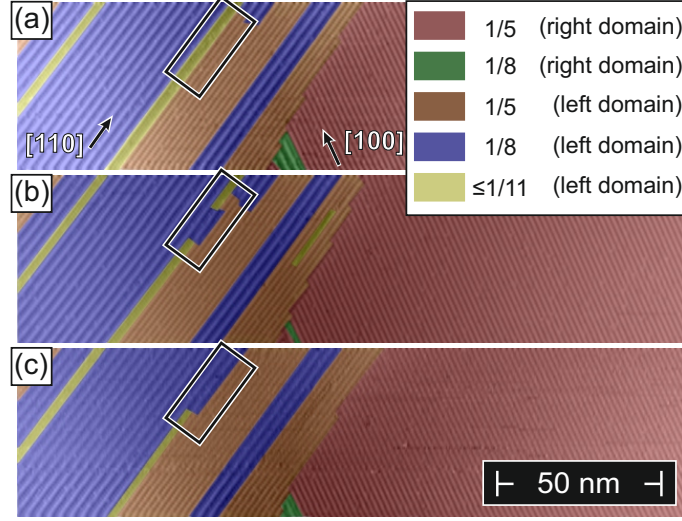


FIG. 5. (Color online) STM data taken on cleaved IrTe₂ at the same sample location at $T = 180$ K after cooling down from RT. For clarity the different domains were color-enhanced. Initially (a), the surface area marked by a rectangle ($\approx 25 \times 12$ nm²) exhibits (8×1) -, (11×1) -, and (5×1) -ordered domains in close proximity. During the time required to complete the scan a switching occurs (b), resulting in the conversion of one (11×1) - and one (5×1) -stripe segment into two (8×1) stripes. As shown by the following image (c) the (11×1) domain in the upper part of the image is eventually annihilated.

Our data indicate that similar processes govern the evolution of solitons below the second phase transition during the cooling process. Namely, switching processes are only allowed if the number of involved atomic rows is consistent in the initial and final state. As a result only a limited subset of switching processes will be possible that may possess relatively large energy barriers. For example, the first match for a transition of (8×1) stripes into $(p \times 1)$ stripes with $p = 3n + 2 > 8$ would be $4 \times (8 \times 1) \rightarrow 1 \times (32 \times 1)$. Since such processes require to overcome a relatively large energy barrier they are extremely rare, especially at low temperatures where thermal activation is low, thereby explaining the wide temperature range over which the second phase transition takes place.

It is well-known that the interplay of interactions may lead to the famous “devil’s staircase” with *infinite* transitions between all possible commensurate (C) modulations.^{41,42} In contrast, the “harmless staircase”, which has mostly been studied by spatially averaging scattering-type measurements,^{43,44} is limited to finite number of first-order transitions be-

tween C phases and was postulated for oscillating soliton interactions.³⁷ Although scattering-type measurements can provide valuable information in reciprocal space if correlation lengths are sufficiently long,^{43,44} they are insufficient to detect non-periodic features, e.g. details of structural defects which potentially pin domain walls.

In this context real-space imaging techniques, such as electron microscopy or STM, significantly extend our capabilities. However, to the best of our knowledge they have so far only been applied to stable C phases.⁴² We are not aware of any study showing details of transitions between competing C phases in real space. We speculate that the CDW-like phase transitions of IrTe₂ observed here possibly represents the first experimental realization of a “harmless staircase” that has been visualized by scanning tunneling microscopy (STM) with high spatial resolution.²⁷

Indeed, when cooling IrTe₂ through the second phase transition at T_S down towards the low-temperature ground state the system has to convert from an almost perfect (5×1) -ordered state (cf. Fig. 1) with alternating $3a^*$ and $2a^*$ units into the (6×1) phase that consists of two slightly different $3a^*$ building blocks. According to our experimental data this is achieved by successively increasing the number of $3a^*$ units between the $2a^*$ boundaries. Density functional theory allows for a qualitative understanding of the energy barriers associated to these processes, thereby explaining the strongly anisotropic domain propagation speeds.

Although limited in principle to a finite number of $(p \times 1)$ -ordered areas, the many pathways possible to realize the transition from the (5×1) -ordered state into the (6×1) phase effectively leads to a highly complex behavior. Since the underlying stripe formation is commensurate with the IrTe₂ lattice, the system closely resembles a “harmless staircase”.³⁷ It remains to be investigated, however, if the second phase transition of IrTe₂ may also be described by an effective “devil’s staircase” at low temperatures where pitch length is large, i.e. for $p = 3n + 2$ domains with $n \gg 2$. Indeed, recent phenomenological modeling of helical antiferroelectric liquid crystalline phases of molecules, the so-called smectic (Sm)- C_α^* structure, in an external electric field revealed a transition from discontinuous steps for short periods to a quasi-continuous transition at long pitch length.⁴⁵

Alternatively, the temperature-dependent processes observed at the IrTe₂ surface may also be discussed in terms of dynamical “freezing” of a first order transition. Dynamical freezing, or kinetic arrest, underscores many sluggish electronic first order transitions or

phase coexistence phenomena which are closely related to the century-old problem, the glass transition.³⁸ In fact, several of the processes observed for IrTe₂, such as the extremely slow relaxation of $p = 3n + 2$ domains towards the (6×1) low temperature ground state, are reminiscent of dynamical freezing. It appears conceivable that the energy landscape of the IrTe₂ surface, that is,—as termed in the review article by Debenedetti and Stillinger³⁸—“the multidimensional surface generated by the systems potential energy”, is so complex that it becomes impossible to sample all available configurations within the time permitted by the cooling rate.

In this context further temperature-dependent studies of the phase transitions of IrTe₂ will be required. For this purpose scanning probe methods will be unsuitable because of their relatively low sampling rate. Instead, we suggest temperature-dependent scattering experiments where the intensities of spots characteristic for the various $p = 3n + 2$ superstructures are carefully studied as functions of the cooling rate. Such experiments may result in an improved understanding of the physical processes which are behind the fascinating behavior of IrTe₂.

IV. SUMMARY

In conclusion, we have carried out a systematic STM study of $(p \times 1)$ stripe modulations at the 2nd phase transition ($T_S \approx 180$ K) in IrTe₂ single crystals. Atomic resolution images of the domain boundaries along different orientations reveal a strongly anisotropic propagation. Our observations qualitatively agree with a first principle analysis of energy barriers, thereby shedding new light on the emerging complex energy landscape which has been discussed in terms of harmless staircase-like transitions and dynamical freezing.

ACKNOWLEDGMENTS

The work at Würzburg was supported by Deutsche Forschungsgemeinschaft within FOR 1162 and by the Alexander von Humboldt Foundation (W.W.). Work at Rutgers was supported by NSF Grants No. DMREF-1233349, No. DMR-0844807 and No. DMR-1506618. The work at Postech was supported by the Max-Planck-POSTECH/KOREA Research Initiative Program (No. 2011-0031558) through the NRF of Korea funded by the Ministry of

- ¹ Y. Wang, G. L. Pascut, B. Gao, T. A. Tyson, K. Haule, V. Kiryukhin, and S.-W. Cheong, *Scientific Reports* **5**, 12268 (2015).
- ² G. L. Pascut, T. Birol, M. J. Gutmann, J. J. Yang, S.-W. Cheong, K. Haule, and V. Kiryukhin, *Phys. Rev. B* **90**, 195122 (2014).
- ³ S. Leoni, *Chemistry A European Journal* **13**, 10022 (2007).
- ⁴ J. C. Schön, K. Doll, and M. Jansen, *Physica Status Solidi (b)* **247**, 23 (2010).
- ⁵ D. Zahn and S. Leoni, *Phys. Rev. Lett.* **92**, 250201 (2004).
- ⁶ S. Leoni and D. Zahn, *Zeitschrift für Kristallographie - Crystalline Materials* **219**, 345 (2004).
- ⁷ D. Zahn and S. Leoni, *Zeitschrift für Kristallographie - Crystalline Materials* **219**, 339 (2004).
- ⁸ D. Zahn, O. Hochrein, and S. Leoni, *Phys. Rev. B* **72**, 094106 (2005).
- ⁹ S. Leoni and R. Nesper, *Acta Crystallographica Section A* **56**, 383 (2000).
- ¹⁰ P. G. Bolhuis, C. Dellago, and D. Chandler, *Faraday Discuss.* **110**, 421 (1998).
- ¹¹ D. Zahn, Y. Grin, and S. Leoni, *Phys. Rev. B* **72**, 064110 (2005).
- ¹² R. Martoňák, *The European Physical Journal B* **79**, 241 (2011).
- ¹³ S. E. Boulfelfel, D. Zahn, O. Hochrein, Y. Grin, and S. Leoni, *Phys. Rev. B* **74**, 094106 (2006).
- ¹⁴ S. E. Boulfelfel and S. Leoni, *Phys. Rev. B* **78**, 125204 (2008).
- ¹⁵ S. E. Boulfelfel, D. Zahn, Y. Grin, and S. Leoni, *Phys. Rev. Lett.* **99**, 125505 (2007).
- ¹⁶ S. Leoni, S. Eddine Boulfelfel, and I. A. Baburin, *Zeitschrift für anorganische und allgemeine Chemie* **637**, 864 (2011).
- ¹⁷ X. He, T. Xu, X. Xu, Y. Zeng, J. Xu, L. Sun, C. Wang, H. Xing, B. Wu, A. Lu, D. Liu, X. Chen, and J. Chu, *Scientific Reports* **4**, 6544 (2014).
- ¹⁸ S. Leoni, R. Ramlau, K. Meier, M. Schmidt, and U. Schwarz, *PNAS* **105**, 19612 (2008).
- ¹⁹ Y. Peng, F. Wang, Z. Wang, A. M. Alsayed, Z. Zhang, A. G. Yodh, and Y. Han, *Nature Materials* **14**, 101 (2015).
- ²⁰ N. Matsumoto, K. Taniguchi, R. Endoh, H. Takano, and S. Nagata, *J. Low Temp. Phys.* **117**, 1129 (1999).
- ²¹ J. J. Yang, Y. J. Choi, Y. S. Oh, A. Hogan, Y. Horibe, K. Kim, B. I. Min, and S.-W. Cheong, *Phys. Rev. Lett.* **108**, 116402 (2012).

- ²² Y. S. Oh, J. J. Yang, Y. Horibe, and S.-W. Cheong, Phys. Rev. Lett. **110**, 127209 (2013).
- ²³ H. Cao, B. C. Chakoumakos, X. Chen, J. Yan, M. A. McGuire, H. Yang, R. Custelcean, H. Zhou, D. J. Singh, and D. Mandrus, Phys. Rev. B **88**, 115122 (2013).
- ²⁴ A. F. Fang, G. Xu, T. Dong, P. Zheng, and N. L. Wang, Sci. Rep. **3**, 1153 (2013).
- ²⁵ A. Kiswandhi, J. S. Brooks, H. B. Cao, J. Q. Yan, D. Mandrus, Z. Jiang, and H. D. Zhou, Phys. Rev. B **87**, 121107 (2013).
- ²⁶ D. Ootsuki, S. Pyon, K. Kudo, M. Nohara, M. Horio, T. Yoshida, A. Fujimori, M. Arita, H. Anzai, H. Namatame, M. Taniguchi, N. L. Saini, and T. Mizokawa, J. Phys. Soc. Jpn. **82**, 093704 (2013).
- ²⁷ P.-J. Hsu, T. Maurer, M. Vogt, J. J. Yang, Y. S. Oh, S.-W. Cheong, M. Bode, and W. Wu, Phys. Rev. Lett. **111**, 266401 (2013).
- ²⁸ G. L. Pascut, K. Haule, M. Gutmann, S. A. Barnett, A. Bombardi, S. Artyukhin, T. Birol, D. Vanderbilt, J. J. Yang, S.-W. Cheong, and V. Kiryukhin, Phys. Rev. Lett. **112**, 086402 (2014).
- ²⁹ Q. Li, W. Lin, J. Yan, X. Chen, A. G. Gianfrancesco, D. J. Singh, D. Mandrus, S. V. Kalinin, and M. Pan, Nat. Comm. **5**, 6358 (2014).
- ³⁰ K. Takubo, R. Comin, D. Ootsuki, T. Mizokawa, H. Wadati, Y. Takahashi, G. Shibata, A. Fujimori, R. Sutarto, F. He, S. Pyon, K. Kudo, M. Nohara, G. Levy, I. S. Elfimov, G. A. Sawatzky, and A. Damascelli, Phys. Rev. B **90**, 081104(R) (2014).
- ³¹ G. L. Pascut, T. Birol, M. J. Gutmann, J. J. Yang, S.-W. Cheong, K. Haule, and V. Kiryukhin, Phys. Rev. B **90**, 195122 (2014).
- ³² H. S. Kim, T.-H. Kim, J. Yang, S.-W. Cheong, and H. W. Yeom, Phys. Rev. B **90**, 201103(R) (2014).
- ³³ J. Dai, K. Haule, J. J. Yang, Y. S. Oh, S.-W. Cheong, and W. Wu, Phys. Rev. B **90**, 235121 (2014).
- ³⁴ D. Mazumdar, K. Haule, J. J. Yang, G. L. Pascut, B. S. Holinsworth, K. R. O'Neal, V. Kiryukhin, S.-W. Cheong, and J. L. Musfeldt, Phys. Rev. B **91**, 041105(R) (2015).
- ³⁵ S. F. Blake, M. D. Watson, A. McCollam, S. Kasahara, R. D. Johnson, A. Narayanan, G. L. Pascut, K. Haule, V. Kiryukhin, T. Yamashita, D. Watanabe, T. Shibauchi, Y. Matsuda, and A. I. Coldea, Phys. Rev. B **91**, 121105(R) (2015).

- ³⁶ A. Glamazda, K.-Y. Choi, P. Lemmens, J. J. Yang, and S.-W. Cheong, *New J. Phys.* **16**, 093061 (2014).
- ³⁷ J. Villain and M. B. Gordon, *J. Phys. C: Solid State Phys.* **13**, 3117 (1980).
- ³⁸ P. G. Debenedetti and F. H. Stillinger, *Nature* **410**, 259 (2001).
- ³⁹ I. Horcas, R. Fernández, J. M. Gómez-Rodríguez, J. Colchero, J. Gómez-Herrero, and A. M. Baro, *Rev. Sci. Instr.* **78**, 013705 (2007).
- ⁴⁰ P. Blaha, K. Schwartz, G. Madsen, D. Kvasnicka, and L. Luitz, *WIEN2k, An Augmented Plane Wave + Local Orbitals Program for Calculating Crystal Properties* (Karlheinz Schwarz, Techn. Universität Wien, Austria 2001. ISBN 3-9501031-1-2).
- ⁴¹ P. Bak, *Rep. Progr. Phys.* **45**, 587 (1982).
- ⁴² M. Hupalo, J. Schmalian, and M. C. Tringides, *Phys. Rev. Lett.* **90**, 216106 (2003).
- ⁴³ M. D. Chinn and S. C. Fain, *Phys. Rev. Lett.* **39**, 146 (1977).
- ⁴⁴ R. M. Fleming, D. E. Moncton, D. B. McWhan, and F. J. DiSalvo, *Phys. Rev. Lett.* **45**, 576 (1980).
- ⁴⁵ B. Rovšek, M. Čepič, and B. Žekš, *Phys. Rev. E* **70**, 041706 (2004).